J. Fluid Mech. (2014), *vol.* 744, *pp.* 329–351. © Cambridge University Press 2014
doi:10.1017/jfm.2014.61

Large-amplitude acoustic streaming

G. P. Chini[1,†], Z. Malecha[1,2] and T. D. Dreeben[3]

[1]Department of Mechanical Engineering, Center for Fluid Physics, and Program in Integrated Applied Mathematics, University of New Hampshire, Durham, NH 03824, USA

[2]Faculty of Mechanical and Power Engineering, Wrocław University of Technology, Wroclaw 50-370, Poland

[3]Corporate Technology, OSRAM SYLVANIA, 71 Cherry Hill Drive, Beverly, MA 01915, USA

(Received 8 February 2013; revised 9 October 2013; accepted 23 January 2014; first published online 12 March 2014)

A mechanism is proposed for the generation of large-amplitude acoustically-driven streaming flows in which time-mean flow speeds are comparable to the instantaneous speed of fluid particles in a high-frequency sound-wave field. Motivated by streaming observed in high-intensity discharge (HID) lamps, two-dimensional flow of a density-stratified ideal gas in a channel geometry is analysed in the asymptotic limit of high-frequency acoustic-wave forcing. Predictions of streaming flow magnitudes based on classical arguments invoking Reynolds stress divergences originating in viscous boundary layers are orders of magnitude too small to account for the observed mean flows. Moreover, classical 'Rayleigh streaming' theory cannot account for the direction of the cellular mean flows often observed in HID lamps. In contrast, the mechanism proposed here, which invokes fluctuating baroclinic torques away from viscous boundary layers and thus is largely independent of viscous effects, can account both for the magnitude and the orientation of the observed streaming flows.

Key words: baroclinic flows, compressible flows, vortex flows

1. Introduction

Steady streaming refers to time-averaged Eulerian flows arising in periodically forced fluid systems; that is, time-averaged flows that emerge in such systems over and above any wave Stokes drift. Streaming flows have been investigated extensively over the last century beginning with Rayleigh's seminal work (Rayleigh 1883). A diverse array of scientific and technological applications involves streaming in a fundamental way, including: measurement of absorption coefficients of common fluids using ultrasonic beams (Piercy & Lamb 1954); heat transfer enhancement to or from solid particles immersed in a fluid (Davidson 1973; Gopinath & Mills 1993); sediment transport and sandbar formation (Mei 1985; Wybrow & Riley 1996); high-frequency ventilation of prematurely born infants (Grotberg 1984; Gaver & Grotberg 1986); the dynamics of the inner ear (Lighthill 1991, 1992); growth of protein crystals (Chung & Trinh 1998); fluid transport aboard spacecraft experiencing 'g-jitter' (Amin 1988; Riley & Trinh 2001); and the performance of high-intensity discharge (HID) lamps (Dreeben & Chini 2011), to cite but a few examples. As explained in the

† Email address for correspondence: greg.chini@unh.edu

https://doi.org/10.1017/jfm.2014.61 Published online by Cambridge University Press

lucid review article by Riley (2001), steady streaming generally requires one of the following three ingredients: (i) the action of an oscillatory *non-conservative* body force; (ii) Reynolds stress divergences (RSDs) arising either in the main body of the fluid owing to gradual viscous attenuation or, more commonly, in thin viscous layers adjacent to no-slip boundaries; or (iii) an oscillating deformable boundary (e.g. a free surface) across which nonlinear kinematic and dynamic conditions hold.

Riley sensibly reserves the use of the term 'acoustic' (rather than 'steady') streaming for flows in which the oscillatory driving is provided by high-frequency sound waves. In the vast majority of applications, acoustic streaming is associated with mechanism (ii). For example, the 'quartz wind' is the mean streaming flow generated by viscous attenuation of an ultrasonic beam in the bulk of a fluid. In contrast, 'Rayleigh streaming' refers to acoustic streaming induced by viscous attenuation of standing acoustic waves in thin boundary layers adjacent to channel walls. The literature, even solely on acoustic streaming, is too vast to review here. Nevertheless, some common features of nearly all acoustically-driven streaming flows that have been described in the literature can be concisely described.

(*a*) Streaming is driven by the divergence of Reynolds stresses induced by rotational acoustic waves, as the Reynolds stresses associated with *irrotational* waves merely modify the time-mean pressure gradient.

(*b*) The required fluctuating vorticity is generated either by dissipation in the bulk flow or, more typically, by viscous stresses in boundary layers.

(*c*) In the high-Strouhal-number limit of interest, $S \gg 1$, where $S \equiv \omega_*/(k_* U_*) \equiv a_*/U_*$ with ω_*, k_* and U_* the (dimensional) frequency, wavenumber and typical particle speed of the acoustic waves and a_* thus the (dimensional) sound speed, unsteady terms in the governing equations are much larger than advection terms.

(*d*) Crucially, streaming velocities are *much smaller* than, more precisely, $O(S^{-1})$ relative to, instantaneous (fluctuating) velocities.

(*e*) The induced streaming velocity at the edge of viscous boundary layers is directed *toward* velocity nodes of the standing acoustic waves.

A natural question is whether there are systems for which some of these conditions either do not apply or may be relaxed. Indeed, the present investigation is strongly motivated by streaming flows in HID lamps, where acoustically generated mean flows are used to significantly improve energy efficiency (e.g. Witting 1978; Stockwald, Kaestle & Weiss 2008; Dreeben 2008) but for which classical streaming arguments utterly fail to explain both qualitative and quantitative streaming features. In HID lamps, light is generated by running an electric current between two electrodes through an ionizable gas contained in a hermetically sealed ceramic or quartz enclosure. Most of the useful light is emitted from a region termed the 'arc' where the gas temperature exceeds $\sim$5000 K. For horizontally running lamps, buoyancy forces cause the arc to bow upward above the lamp axis. By modulating the current at an acoustic eigenfrequency, lighting engineers have demonstrated that acoustic streaming flows can be generated that are sufficiently intense to overcome the $O(10)$ cm s^{-1} buoyancy-driven flows. Dreeben & Chini (2011) show that neither the magnitude nor the direction of the acoustically-driven streaming flows exhibited in observations and simulations of HID lamps is consistent with predictions based on classical acoustic streaming theory. In a suite of numerical simulations, these authors found that the acoustically generated streaming flows could reach 0.3 m s^{-1}, a significant fraction of the 3.0 m s^{-1} amplitude of the acoustic wave velocity fluctuations. Moreover, near the arc tube walls, the streaming flow was directed *away* from the velocity nodes of

https://doi.org/10.1017/jfm.2014.61 Published online by Cambridge University Press

the (approximately) standing acoustic waves. In contrast, classical Rayleigh streaming analysis predicts a maximum streaming velocity less than 0.01 m s^{-1}, with the mean flow directed toward the velocity nodes.

A primary theme of the present study is that large-amplitude streaming flows, having a magnitude commensurate with that of the driving oscillatory flow, independently of the (large) oscillation frequency, may be realized when the fluctuating vorticity responsible for inducing the mean motion is *not* generated by viscous agencies. In this context, we note that Riley & Trinh (2001), building on the earlier work of Amin (1988) and Merkin (1967), demonstrated a similar result. While Riley & Trinh (2001) treat the case of an imposed, non-conservative body force in the form of g-jitter-induced buoyancy fluctuations, we consider a scenario not specifically contemplated before: large-amplitude *acoustic* streaming enabled by spatial variations in the mean density distribution.

Our thesis is that the RSDs driving the strong streaming flows in HID lamps are associated with vorticity fluctuations produced by acoustic wave particle displacements, not in viscous boundary layers, but in the strongly density stratified interior of the flow. Indeed, a several thousand degree (Kelvin) temperature difference exists between the arc and the wall of the lamp, corresponding to a factor of five density variation within the gas (Dreeben & Chini 2011). This provides a source of fluctuating $O(1)$ vorticity (when normalized by U_* and H_*, a typical 'outer' flow length scale) throughout the domain.

The outline of the remainder of the paper is as follows. Motivated by the inapplicability of conditions of (*b*), (*d*), and (*e*) in HID lamps (Dreeben & Chini 2011), we formulate in § 2 and analyse in § 3 a model problem in which acoustically-driven, fluctuating *baroclinic* torques within the bulk fluid are responsible for driving strong streaming flows. As for other streaming scenarios, this problem is analysed in the asymptotic limit of high-frequency forcing, but the result here is a novel set of wave/mean-flow interaction equations governing the fully two-way coupling between the high-frequency acoustic waves and the slowly evolving, large-amplitude streaming flows. In this context, and henceforth, it should be noted that the term *large-amplitude* (or *strong*) refers specifically to a streaming flow having a magnitude *relative* to that of the fluctuating flow that is asymptotically larger than the classical $O(S^{-1})$ value. The two-way coupling between the waves and mean flows they drive makes further analytical progress difficult for arbitrary values of the streaming Péclet number Pe_s (defined in § 3). However, as demonstrated in § 4, further progress can be made in the limit $Pe_s \ll 1$ principally because the streaming flow then does not modify the leading-order wave dynamics. For analytical tractability, this limit is exploited in § 4. To relax this restriction and to corroborate the basic tenets of our theory, in § 5 we complement our asymptotic analysis with direct numerical simulations (DNS) of the full (non-asymptotic) model equations. Our key findings are summarized in § 6.

2. Problem formulation

To explore the efficacy of the proposed streaming mechanism, we consider a model problem involving two-dimensional (2D) flow of an ideal gas in a long thin channel of width $2H_*$. A steady internal heat source Q_* maintains a cross-channel (i.e. $\tilde{y}$-varying) temperature, and hence density, distribution. Nevertheless, buoyancy effects are not included in this analysis, as these are not central to the proposed streaming mechanism. We investigate the possibility that streaming flows can be driven by standing high-frequency acoustic waves with (for definiteness) velocity

https://doi.org/10.1017/jfm.2014.61 Published online by Cambridge University Press

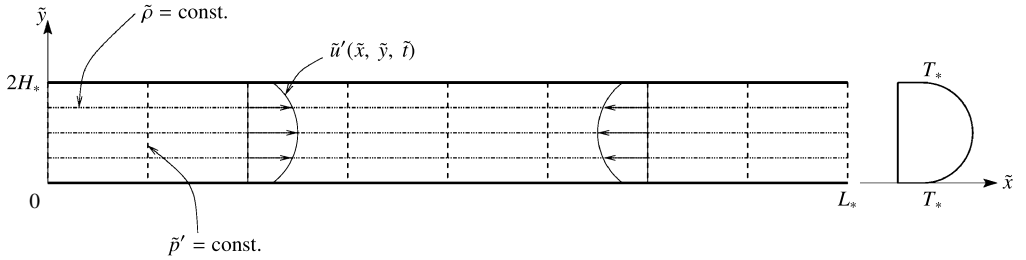


FIGURE 1. Schematic of standing acoustic waves in an internally-heated channel. The background temperature profile, shown to the right, leads to a steady cross-channel density variation in which less dense gas is located near the channel centreline. The fluctuating pressure ($\tilde{p}'$) gradient driving the acoustic waves is approximately uniform across the channel. Consequently, gas in the centre of the channel experiences greater accelerations than does the gas near the channel walls at $\tilde{y} = 0$ and $\tilde{y} = 2H_*$, and the fluctuating $\tilde{x}$-velocity component $\tilde{u}'(\tilde{x}, \tilde{y}, \tilde{t})$ is sheared in the $\tilde{y}$ direction: the acoustic waves are rotational. Vorticity is generated by fluctuating baroclinic torques, because the leading-order isobars (dashed vertical lines) are orthogonal to the steady isopycnals (dashed-dotted horizontal lines) induced by the heat source.

nodes at the upstream and downstream ends of the channel, located at $\tilde{x} = 0$ and $\tilde{x} = L_* \equiv 2\pi/k_*$, respectively. As shown in figure 1, the instantaneous isobars associated with the leading-order acoustic wave pressure fluctuations are perpendicular to isopycnals associated with the imposed (steady) background temperature distribution, a configuration that clearly favours baroclinic production of fluctuating vorticity. For simplicity, the specific heat coefficients at constant volume and pressure, c_v and c_p, respectively, the dynamic viscosity μ, and the thermal conductivity κ are presumed to be constants, and expansion damping (Batchelor 1973, p. 154) and viscous heating are neglected.

Under the given assumptions, the governing dimensional equations are

$$\tilde{\rho}\left[\partial_{\tilde{t}}\tilde{\boldsymbol{u}} + \left(\tilde{\boldsymbol{u}}\cdot\tilde{\nabla}\right)\tilde{\boldsymbol{u}}\right] = -\tilde{\nabla}\tilde{p} + \mu\left[\tilde{\nabla}^2\tilde{\boldsymbol{u}} + \tfrac{1}{3}\tilde{\nabla}\left(\tilde{\nabla}\cdot\tilde{\boldsymbol{u}}\right)\right], \tag{2.1}$$

$$\partial_{\tilde{t}}\tilde{\rho} + \partial_{\tilde{x}}(\tilde{\rho}\tilde{u}) + \partial_{\tilde{y}}(\tilde{\rho}\tilde{v}) = 0, \tag{2.2}$$

$$\tilde{\rho}c_v\left[\partial_{\tilde{t}}\tilde{T} + \left(\tilde{\boldsymbol{u}}\cdot\tilde{\nabla}\right)\tilde{T}\right] = -\tilde{p}\left(\tilde{\nabla}\cdot\tilde{\boldsymbol{u}}\right) + \kappa\tilde{\nabla}^2\tilde{T} + Q_*, \tag{2.3}$$

$$\tilde{p} = \tilde{\rho}R\tilde{T}. \tag{2.4}$$

In (2.1)–(2.4), tildes refer to dimensional variables; $\tilde{\rho}$ is the gas density; $\tilde{\boldsymbol{u}}$ is the gas velocity, with components $\tilde{u}$ and $\tilde{v}$ in the $\tilde{x}$ and $\tilde{y}$ directions (i.e. parallel and perpendicular to the channel), respectively; $\tilde{p}$ is the gas pressure; $\tilde{T}$ is the gas temperature; and R is the gas constant. A specified, space ($\tilde{x}$, $\tilde{y}$) and time ($\tilde{t}$) independent heat source Q_* is used to crudely model the mean temperature distribution in a HID lamp. In the absence of fluid motion, Q_* is defined so that

$$\tilde{T} = \tilde{T}_B(\tilde{y}) \equiv T_* + \Delta\Theta_*\left(\frac{\tilde{y}}{H_*}\right)\left(2 - \frac{\tilde{y}}{H_*}\right). \tag{2.5}$$

Here, $\tilde{T}_B$ refers to the 'basic-state' (or 'background') temperature distribution and, from (2.3), the temperature difference $\Delta\Theta_*$ between the centreline value and T_*

https://doi.org/10.1017/jfm.2014.61 Published online by Cambridge University Press

(i.e. the dimensional wall temperature) is $H_*^2 Q_*/(2\kappa)$. Associated with this temperature distribution and the constant background pressure distribution $\tilde{p}_B = p_*$ (consistent with (2.1) in the absence of fluid motion) is the background density distribution

$$\tilde{\rho}_B(\tilde{y}) = \frac{p_*}{R\tilde{T}_B(\tilde{y})}. \tag{2.6}$$

Finally, the basic state velocity field $\tilde{\boldsymbol{u}}_B = \boldsymbol{0}$.

Equations (2.1)–(2.4) are supplemented with the following boundary conditions. Along the lower channel wall, which is coincident with the plane $\tilde{y} = 0$, we impose zero normal flow ($\tilde{v} = 0$), zero tangential stress ($\partial_{\tilde{y}}\tilde{u} = 0$) and constant heat-flux ($\partial_{\tilde{y}}\tilde{T} = 2\Delta\Theta_*/H_*$) conditions. The latter constraints are intentionally chosen to suppress viscous and thermal boundary-layer effects and thereby highlight the largely inviscid nature of the proposed streaming mechanism. The presumed symmetries of the solutions of interest enable us to separately analyse the flow in the lower (or upper) half of the channel. Thus, along the channel centreline $\tilde{y} = H_*$, we impose the symmetry conditions: $\tilde{v} = 0$, $\partial_{\tilde{y}}\tilde{u} = 0$ and $\partial_{\tilde{y}}\tilde{T} = 0$. All fields are assumed to be L_*-periodic in the $\tilde{x}$ direction. Since the density is algebraically slaved to the pressure and temperature through the ideal gas equation of state (2.4), we do not specify independent boundary conditions on $\tilde{\rho}(\tilde{x}, \tilde{y}, \tilde{t})$.

We proceed by decomposing the total temperature and pressure into basic state contributions plus perturbations about those background profiles; i.e.

$$\tilde{T}(\tilde{x}, \tilde{y}, \tilde{t}) \equiv \tilde{T}_B(\tilde{y}) + \tilde{\Theta}(\tilde{x}, \tilde{y}, \tilde{t}), \tag{2.7}$$

$$\tilde{p}(\tilde{x}, \tilde{y}, \tilde{t}) \equiv p_* + \tilde{\pi}(\tilde{x}, \tilde{y}, \tilde{t}). \tag{2.8}$$

Next, we substitute these decompositions into the governing equations and boundary conditions and non-dimensionalize the resulting system. We scale $\tilde{x}$ with k_*^{-1}; $\tilde{y}$ with H_*; $\tilde{T}$ with the wall temperature T_*; $\tilde{p}$ with the background pressure p_*; and $\tilde{\rho}$ with $\rho_* \equiv p_*/(RT_*)$. In the absence of stratification, the temperature would be uniform and equal to T_*, and the corresponding sound speed $a_* \equiv \sqrt{(c_p/c_v)RT_*} \equiv \omega_*/k_*$. Hence, we scale $\tilde{u}$ with the unstratified sound speed a_*; $\tilde{v}$ with $(k_*H_*)a_*$; and time $\tilde{t}$ with ω_*^{-1}.

With these scalings, the dimensionless governing equations become

$$\rho[\partial_t u + (\boldsymbol{u}\cdot\nabla)u] = -\frac{1}{\gamma}\partial_x\pi + \frac{1}{SRe}\left[\left(\partial_x^2 + \frac{1}{\delta^2}\partial_Y^2\right)u + \frac{1}{3}\partial_x(\nabla\cdot\boldsymbol{u})\right], \tag{2.9}$$

$$\rho[\partial_t V + (\boldsymbol{u}\cdot\nabla)V] = -\frac{1}{\delta^2\gamma}\partial_Y\pi + \frac{1}{SRe} \times \left[\left(\partial_x^2 + \frac{1}{\delta^2}\partial_Y^2\right)V + \frac{1}{3\delta^2}\partial_Y(\nabla\cdot\boldsymbol{u})\right], \tag{2.10}$$

$$\partial_t\rho + \partial_x(\rho u) + \partial_Y(\rho V) = 0, \tag{2.11}$$

$$\partial_t\Theta + (\boldsymbol{u}\cdot\nabla)\Theta + V\frac{\mathrm{d}T_B}{\mathrm{d}Y} = (1-\gamma)(T_B+\Theta)(\nabla\cdot\boldsymbol{u}) + \frac{\gamma}{\rho SPe}\left[\partial_x^2 + \frac{1}{\delta^2}\partial_Y^2\right]\Theta, \tag{2.12}$$

$$\rho = \frac{1+\pi}{T_B+\Theta}. \tag{2.13}$$

In (2.9)–(2.13), all variables are now dimensionless; Y and V are the scaled cross-channel coordinate and velocity component, respectively; $\boldsymbol{u} = (u, \delta V)$; and

https://doi.org/10.1017/jfm.2014.61 Published online by Cambridge University Press

Variable	Scale	Value
x	k_*^{-1}	10 mm
y	H_*	1 mm
t	ω_*^{-1}	10^{-5} s
u	a_*	1000 m s^{-1}
v	$(k_*H_*)\,a_*$	100 m s^{-1}
ρ	ρ_*	1 kg m^{-3}
T	T_*	1000 K
P	$\rho_* RT_*$	1000 kPa

TABLE 1. Dimensional scales, including typical values, used to render the governing equations dimensionless and to motivate the distinguished limit used in the asymptotic analysis.

$\nabla = (\partial_x,\ \delta^{-1}\partial_Y)$. In addition to the previously defined Strouhal number S, five other dimensionless parameters appear in this system: $\delta = k_*H_*$ is a measure of the aspect ratio of the channel; $\gamma = c_p/c_v$ is the $O(1)$ specific heat ratio; and $Re = (\rho_* U_*)/(k_*\mu)$ and $Pe = (\rho_* c_p U_*)/(k_*\kappa)$ are the Reynolds and Péclet numbers based on a typical fluctuation velocity U_*. In (2.12) and (2.13), the dimensionless background temperature distribution

$$T_B(Y) = 1 + (\Gamma Y)(2 - Y), \tag{2.14}$$

where $\Gamma \equiv \Delta\Theta_*/T_*$ is an additional dimensionless parameter giving the ratio of the imposed temperature difference between the channel centreline and wall to the wall temperature itself. The problem formulation is completed by augmenting (2.9)–(2.12) with the following boundary conditions along the lower wall and channel centreline:

$$V(x, Y = 0, t) = 0, \quad \partial_Y u(x, Y = 0, t) = 0, \quad \partial_Y \Theta(x, Y = 0, t) = 0; \tag{2.15}$$

$$V(x, Y = 1, t) = 0, \quad \partial_Y u(x, Y = 1, t) = 0, \quad \partial_Y \Theta(x, Y = 1, t) = 0. \tag{2.16}$$

Finally, all dimensionless fields are 2π-periodic in the x coordinate.

3. Asymptotic analysis: wave/mean-flow interaction equations

We perform an asymptotic analysis of the system (2.9)–(2.16) by considering the physically relevant high-frequency limit, $S \gg 1$, presuming dissipative effects to be suitably small: $Re \equiv SRe_s$ and $Pe \equiv SPe_s$, where Re_s and Pe_s will be seen to be the streaming Reynolds and Péclet numbers. Motivated by the discussion at the end of § 1 and in § 2 (see figure 1), we also make a small-aspect-ratio approximation, $\delta \equiv S^{-1/2}h$, where $h = O(1)$. This approximation, which is not unreasonable for longitudinal (as opposed to azimuthal) acoustic waves in HID lamps, ensures that the leading-order pressure distribution is uniform across the channel and that the leading-order acoustic wave particle displacements are oriented in the x direction. Tables 1 and 2 summarize both the dimensional scales and the non-dimensional parameters used in this analysis.

Although we scale velocities using the (unstratified) sound speed, typical acoustic wave particle speeds in HID lamps are very much smaller than a_*; specifically, we take $(u,\ V) = O(S^{-1})$. Thus, streaming arises as a *slow* cumulative effect of weak

https://doi.org/10.1017/jfm.2014.61 Published online by Cambridge University Press

Parameter	Definition	Scaling
Wave amplitude S^{-1}	U_*/a_*	$S^{-1} \ll 1$
Aspect ratio δ	$k_* H_*$	$\delta \equiv S^{-1/2} h$
Temperature gradient Γ	$\Delta\Theta_*/T_*$	$\Gamma = O(1)$
Reynolds number Re	$\rho_* U_*/(k_*\mu)$	$Re \equiv SRe_s$
Péclet number Pe	$\rho_* c_p U_*/(k_*\kappa)$	$Pe \equiv SPe_s$
Specific heat ratio γ	c_p/c_v	$\gamma = O(1)$

TABLE 2. Dimensionless parameters arising in (2.9)–(2.13) and used in the asymptotic analysis.

nonlinearity. We explicitly recognize the occurrence of fast acoustic-wave and slow streaming dynamics by formally introducing two time scales $\tau \equiv t$ and $T \equiv S^{-1}t$ so that generic dependent variable $f(x, Y, t) \to f(x, Y, \tau, T)$ and $\partial_t f \to \partial_\tau f + S^{-1}\partial_T f$. To separate the high-frequency acoustic wave motions from the mean streaming flows, we also introduce the 'fast' time average $\overline{f} \equiv (\omega/2n\pi)\int_\tau^{\tau+2n\pi/\omega} f(x, Y, s, T)\mathrm{d}s$ for sufficiently large positive integer n and function f which is $2\pi/\omega$-periodic in τ. Note that the dimensionless wave frequency ω differs from unity owing to the background density stratification. With this averaging operation, $f = \overline{f}(x, Y, T) + f'(x, Y, \tau, T)$, where the prime here refers to a fluctuation with zero (fast-time) mean.

We proceed by expanding

$$(u, V) \sim S^{-1}(u_1, V_1) + S^{-2}(u_2, V_2) + \cdots, \tag{3.1}$$

$$\pi \sim S^{-1}\pi_1 + S^{-2}\pi_2 + \cdots, \tag{3.2}$$

$$\Theta \sim \Theta_0 + S^{-1}\Theta_1 + \cdots, \tag{3.3}$$

$$\rho \sim \rho_0 + S^{-1}\rho_1 + \cdots. \tag{3.4}$$

In view of the state equation (2.13) and expansion (3.1), the x momentum equation (2.9) indicates that the leading-order contribution to π arises at $O(S^{-1})$, in accord with (3.2). However, in the presence of strong streaming flows $(\bar{u}, \bar{V}) = O(S^{-1})$, i.e. comparable to (u', V'), the advection of the background temperature distribution $T_B(Y)$ by the leading-order wall-normal streaming velocity $\bar{V}_1$ may be expected to induce $O(1)$ modifications $\bar{\Theta}_0$ to the background temperature, itself, on $O(S)$ (i.e. slow) time scales. Hence, the expansion (3.3) for Θ includes an $O(1)$ component Θ_0. In fact, substitution into the energy equation (2.12) at leading order leads to the requirement $\partial_\tau \Theta_0 = 0$, implying

$$\Theta_0 = \bar{\Theta}_0(x, Y, T). \tag{3.5}$$

Similarly, the $O(1)$ continuity equation requires $\partial_\tau \rho_0 = 0$, so

$$\rho_0 = \bar{\rho}_0(x, Y, T). \tag{3.6}$$

Finally, substituting these expansions into the state equation (2.13) and collecting terms at $O(1)$ yields

$$\rho_0 = \bar{\rho}_0 = \frac{1}{T_B + \bar{\Theta}_0} \tag{3.7}$$

https://doi.org/10.1017/jfm.2014.61 Published online by Cambridge University Press

and $\rho_0' \equiv 0$, in accord with (3.6). At $O(S^{-1})$, the same equation requires

$$\bar{\pi}_1 = \bar{\rho}_1(T_B + \bar{\Theta}_0) + \bar{\rho}_0\bar{\Theta}_1 \tag{3.8}$$

and

$$\pi_1' = \rho_1'(T_B + \bar{\Theta}_0) + \bar{\rho}_0\Theta_1'. \tag{3.9}$$

Returning to the x momentum equation (2.9), we obtain at $O(S^{-1})$

$$\partial_x\bar{\pi}_1 = 0, \tag{3.10}$$

$$\bar{\rho}_0\partial_\tau u_1' = -\frac{1}{\gamma}\partial_x\pi_1'. \tag{3.11}$$

At $O(S^{-2})$,

$$\bar{\rho}_0(\partial_T u_1 + \partial_\tau u_2) + \rho_1\partial_\tau u_1 + \bar{\rho}_0(u_1\partial_x u_1 + V_1\partial_Y u_1) = -\frac{1}{\gamma}\partial_x\pi_2 + \frac{1}{Re_s h^2}\partial_Y^2 u_1. \tag{3.12}$$

Fast-time averaging this equation yields an evolution equation for the x-component of the mean flow:

$$\begin{aligned}\bar{\rho}_0[\partial_T\bar{u}_1 + \bar{u}_1\partial_x\bar{u}_1 + \bar{V}_1\partial_Y\bar{u}_1] = &-\frac{1}{\gamma}\partial_x\bar{\pi}_2 - \overline{\rho_1'\partial_\tau u_1'} \\ &- \bar{\rho}_0\left[\overline{u_1'\partial_x u_1'} + \overline{V_1'\partial_Y u_1'}\right] + \frac{1}{Re_s h^2}\partial_Y^2\bar{u}_1.\end{aligned} \tag{3.13}$$

At leading order, the Y-momentum equation (2.10) gives $\partial_Y\pi_1 = 0$, implying that the fast-time mean pressure at $O(S^{-1})$, $\bar{\pi}_1$, is strictly constant, upon using (3.10). Owing to the small aspect ratio of the channel, we also conclude that the fluctuating $O(S^{-1})$ pressure π_1' is Y-independent:

$$\partial_Y\pi_1' = 0. \tag{3.14}$$

At next order, (2.10) requires

$$\bar{\rho}_0\partial_\tau V_1 = -\frac{1}{\gamma h^2}\partial_Y\pi_2, \tag{3.15}$$

from which we deduce that the $O(S^{-2})$ mean pressure is also independent of the wall-normal coordinate; namely

$$\partial_Y\bar{\pi}_2 = 0. \tag{3.16}$$

(Note that the corresponding fluctuation equation, $\partial_Y\pi_2' = -\gamma h^2\bar{\rho}_0\partial_\tau V_1'$ should be interpreted as an equation for $\pi_2'(x, Y, \tau, T)$, *given* $V_1'(x, Y, \tau, T)$.)

Averaging the $O(S^{-1})$ continuity equation

$$\partial_\tau\rho_1 + \partial_T\bar{\rho}_0 + \partial_x(\bar{\rho}_0 u_1) + \partial_Y(\bar{\rho}_0 V_1) = 0 \tag{3.17}$$

yields

$$\partial_T\bar{\rho}_0 + \partial_x(\bar{\rho}_0\bar{u}_1) + \partial_Y(\bar{\rho}_0\bar{V}_1) = 0. \tag{3.18}$$

https://doi.org/10.1017/jfm.2014.61 Published online by Cambridge University Press

Subtracting (3.18) from (3.17) yields an equation for the fluctuating density:

$$\partial_\tau \rho_1' + \partial_x(\bar{\rho}_0 u_1') + \partial_Y(\bar{\rho}_0 V_1') = 0. \tag{3.19}$$

Finally, the energy equation (2.12) at $O(S^{-1})$ is

$$\partial_\tau \Theta_1 + \partial_T \bar{\Theta}_0 + u_1 \partial_x \bar{\Theta}_0 + V_1 \left(\partial_Y \bar{\Theta}_0 + \frac{\mathrm{d}T_B}{\mathrm{d}Y}\right) = (1-\gamma)(T_B + \bar{\Theta}_0)(\partial_x u_1 + \partial_Y V_1) + \frac{\gamma}{\bar{\rho}_0 Pe_s h^2} \partial_Y^2 \bar{\Theta}_0. \tag{3.20}$$

Averaging this equation yields

$$\partial_T \bar{\Theta}_0 + \bar{u}_1 \partial_x \bar{\Theta}_0 + \bar{V}_1 \left(\partial_Y \bar{\Theta}_0 + \frac{\mathrm{d}T_B}{\mathrm{d}Y}\right) = (1-\gamma)(T_B + \bar{\Theta}_0)(\partial_x \bar{u}_1 + \partial_Y \bar{V}_1) + \frac{\gamma}{\bar{\rho}_0 Pe_s h^2} \partial_Y^2 \bar{\Theta}_0, \tag{3.21}$$

and subtracting this averaged equation from the instantaneous version gives

$$\partial_\tau \Theta_1' + u_1' \partial_x \bar{\Theta}_0 + V_1' \left(\partial_Y \bar{\Theta}_0 + \frac{\mathrm{d}T_B}{\mathrm{d}Y}\right) = (1-\gamma)(T_B + \bar{\Theta}_0)(\partial_x u_1' + \partial_Y V_1'). \tag{3.22}$$

Collecting these results yields the leading-order wave/mean-flow interaction system. The leading-order acoustic wave dynamics are governed by (3.11), (3.14), (3.19), (3.22) and (3.9):

$$\partial_\tau(\bar{\rho}_0 u_1') = -\frac{1}{\gamma}\partial_x \pi_1', \tag{3.23}$$

$$\partial_Y \pi_1' = 0, \tag{3.24}$$

$$\partial_\tau \rho_1' + \partial_x(\bar{\rho}_0 u_1') + \partial_Y(\bar{\rho}_0 V_1') = 0, \tag{3.25}$$

$$\partial_\tau \Theta_1' + u_1' \partial_x \bar{\Theta}_0 + V_1' \left(\partial_Y \bar{\Theta}_0 + \frac{\mathrm{d}T_B}{\mathrm{d}Y}\right) = (1-\gamma)(T_B + \bar{\Theta}_0)(\partial_x u_1' + \partial_Y V_1'), \tag{3.26}$$

$$\pi_1' = \rho_1'(T_B + \bar{\Theta}_0) + \bar{\rho}_0 \Theta_1'. \tag{3.27}$$

Thus, the acoustic waves are non-dissipative, two-dimensional and two-component; that is, $V_1' \neq 0$ in the presence of background stratification. Briefly, since (3.24) implies $\pi_1' = \pi_1'(x, \tau, T)$, (3.23) requires that the leading-order fluctuating x-directed mass flux

$$m_1' \equiv \bar{\rho}_0 u_1' = m_1'(x, \tau, T). \tag{3.28}$$

Even if $\bar{\Theta}_0 = 0$ (which is not true in general, but see § 4), the leading-order temperature fluctuations inherit a Y-dependence when T_B varies with Y. Since the leading-order pressure fluctuations are independent of Y, the equation of state (3.27) indicates that the leading-order density fluctuations generally do depend on Y. Recalling that m_1' is Y-independent, (3.25) then requires that a fluctuating wall-normal velocity is induced to ensure that mass conservation is satisfied. Physically, the stratification causes the largely x-directed wave-induced particle motions to refract, inducing a Y velocity component.

https://doi.org/10.1017/jfm.2014.61 Published online by Cambridge University Press

The leading-order mean equations governing the induced streaming flow are given by (3.13), (3.16), (3.18), (3.21) and (3.7):

$$\bar{\rho}_0\left[\partial_T\bar{u}_1+\bar{u}_1\partial_x\bar{u}_1+\bar{V}_1\partial_Y\bar{u}_1\right] = -\frac{1}{\gamma}\partial_x\bar{\pi}_2-\partial_x(\bar{\rho}_0\overline{u_1'^2})-\partial_Y(\bar{\rho}_0\overline{u_1'V_1'}) + \frac{1}{Re_sh^2}\partial_Y^2\bar{u}_1, \tag{3.29}$$

$$\partial_Y\bar{\pi}_2 = 0, \tag{3.30}$$

$$\partial_T\bar{\rho}_0+\partial_x(\bar{\rho}_0\bar{u}_1)+\partial_Y(\bar{\rho}_0\bar{V}_1) = 0, \tag{3.31}$$

$$\partial_T\bar{\Theta}_0+\bar{u}_1\partial_x\bar{\Theta}_0+\bar{V}_1\left(\partial_Y\bar{\Theta}_0+\frac{\mathrm{d}T_B}{\mathrm{d}Y}\right) = (1-\gamma)(T_B+\bar{\Theta}_0)(\partial_x\bar{u}_1+\partial_Y\bar{V}_1) + \left(\frac{\gamma}{Pe_sh^2}\right)\frac{1}{\bar{\rho}_0}\partial_Y^2\bar{\Theta}_0, \tag{3.32}$$

$$\bar{\rho}_0 = \frac{1}{T_B+\bar{\Theta}_0}, \tag{3.33}$$

where the fluctuation continuity equation (3.25) has been used to simplify the RSDs on the right-hand side of (3.29).

Equations (3.23)–(3.33) comprise a novel wave/mean-flow interaction system. Owing to the potential for strong mean flows, streaming-induced modifications to the background temperature field, captured by the terms involving $\bar{\Theta}_0$, occur on time scales long compared with the inverse acoustic wave frequency but ultimately feed back upon the leading-order acoustic wave dynamics. The streaming, itself, can only be driven by the RSDs in the mean x momentum equation (3.29). In the absence of these terms, it is readily confirmed that no mean flow is driven: $\bar{u}_1=\bar{V}_1=\bar{\pi}_2=\bar{\Theta}_0\equiv 0$ and $\bar{\rho}_0=1/T_B(Y)$ then satisfies (3.29)–(3.33). In fact, even if present, the RSDs must have *non-zero curl* to drive a mean flow; otherwise, the Reynolds stresses merely induce a modification to the mean pressure gradient (Riley 2001). Thus, in view of (3.30), the crucial issue is whether the Y-derivative of the RSDs in (3.29) is non-zero. If so, a streaming flow must arise at $O(S^{-1})$; i.e. the magnitude of this streaming flow is asymptotically of the same order as that of the fluctuations that drive it.

In the next section, we exploit the limit of small streaming Péclet number Pe_s to demonstrate the existence and nature of this large-amplitude acoustic streaming. The key simplification that enables further analytical progress is that steady streaming solutions with $\bar{\Theta}_0=0$ can be found when $S^{-1}\ll Pe_s\ll 1$. Conversely, for $Pe_s\geqslant O(1)$, $\bar{\Theta}_0\neq 0$, and there is the potential for fully two-way coupling between the acoustic waves and streaming flows. In HID lamps, for example, driven acoustic waves can move in and out of resonance as the strong streaming flow induced by the waves alters the background temperature profile and hence the resonant wave speed. Although of considerable interest, fully two-way coupling complicates the determination of the leading-order acoustic wave dynamics: specifically, although $\bar{\Theta}_0(x,\,Y,\,T)$ remains effectively fixed during the fast-time evolution of the acoustic waves, which therefore remain essentially linear, the fluctuation equations are non-autonomous in x and non-separable in x and Y owing to the x and Y dependence of the leading-order mean temperature field. Given our objective, this constitutes a level of complexity that is undesirable and ultimately beyond the scope of the present investigation. Hence, we proceed analytically by exploiting the small-Pe_s limit in § 4 and, subsequently, in § 5, we perform DNS of the original system (2.9)–(2.13) for $O(1)$ values of

https://doi.org/10.1017/jfm.2014.61 Published online by Cambridge University Press

Pe_s to confirm the basic tenets of our theory. Nevertheless, we emphasize that it should be *far* less computationally expensive to numerically integrate the asymptotic wave/mean-flow interaction system (3.23)–(3.33) using e.g. an algorithm akin to the heterogeneous multiscale method (Abdulle & Weinan 2003; Malecha, Chini & Julien 2013) than it is to perform DNS.

4. The limit of small streaming Péclet number

4.1. *The Rayleigh–Nyborg–Westervelt limit:* $S^{-1} \ll (Re_s, Pe_s) \ll 1$

For gases with $O(1)$ Prandtl number, the limit of small Pe_s also corresponds to the so-called Rayleigh–Nyborg–Westervelt (RNW) limit (Lighthill 1978) of small streaming Reynolds number Re_s (Rayleigh 1883; Nyborg 1953; Westervelt 1953). Examination of the mean energy equation (3.32) and boundary conditions (2.15)–(2.16) suggests that in this limit steady streaming solutions can exist with $\bar{\Theta}_0 = 0$. (To be precise, it is possible that $\bar{\Theta}_0 = \bar{\Theta}_0(x)$, but this term appears to be unforced in the RNW limit.) Then, from (3.33),

$$\bar{\rho}_0 = \frac{1}{T_B(Y)}, \tag{4.1}$$

effectively decoupling the waves from the mean flow, since $T_B(Y) = 1 + \Gamma Y(2 - Y)$ is specified. Balancing viscous diffusion of mean momentum with the Reynolds stress forcing in (3.29) yields

$$\frac{1}{h^2}\partial_Y^2 \check{u}_1 = \frac{1}{\gamma}\partial_x \bar{\pi}_2 + \partial_x\left(\bar{\rho}_0 \overline{u_1'^2}\right) + \partial_Y\left(\bar{\rho}_0 \overline{u_1' V_1'}\right), \tag{4.2}$$

where $\check{u}_1 \equiv \bar{u}_1/Re_s = O(1)$. Taking the Y-derivative of this equation, using (3.30), gives

$$\frac{1}{h^2}\partial_Y^2 \check{\Omega} = -\partial_Y\left[\partial_x\left(\frac{1}{T_B}\overline{u_1'^2}\right) + \partial_Y\left(\frac{1}{T_B}\overline{u_1' V_1'}\right)\right]. \tag{4.3}$$

Here, $\check{\Omega} \equiv -\partial_Y \check{u}_1$ is asymptotic to the mean z-vorticity component. For steady streaming $\partial_T \bar{\rho}_0 = 0$ and a mean stream function $\check{\Psi}$ can also be introduced: $\bar{\rho}_0 \check{u}_1 \equiv \partial_Y \check{\Psi}$ and $\bar{\rho}_0 \check{V}_1 \equiv -\partial_x \check{\Psi}$, where $\check{V}_1 \equiv \bar{V}_1/Re_s = O(1)$. Since $\check{\Omega} = -\partial_Y[(1/\bar{\rho}_0)\partial_Y \check{\Psi}]$,

$$\partial_Y\left[T_B(Y)\partial_Y \check{\Psi}\right] = -\check{\Omega}. \tag{4.4}$$

Equations (4.3) and (4.4) constitute a closed system for the mean flow, once the Y-derivative of the RSDs in (4.3) is determined.

The fluctuation equations (3.23)–(3.27) with $\bar{\rho}_0 = 1/T_B(Y)$ can be manipulated to obtain an equation for the leading-order x-directed mass flux:

$$\partial_\tau^2 m_1' = T_B(Y)\partial_x^2 m_1' + \partial_Y(\partial_x V_1'). \tag{4.5}$$

Since $m_1'(x, \tau)$ is independent of Y and $V_1'(x, Y, \tau)$ vanishes at $Y = 0$ and $Y = 1$, (4.5) can be readily integrated across the half-channel to obtain

$$\partial_\tau^2 m_1' = \left(1 + \frac{2\Gamma}{3}\right)\partial_x^2 m_1', \tag{4.6}$$

https://doi.org/10.1017/jfm.2014.61 Published online by Cambridge University Press

upon substituting $T_B(Y) = 1 + \Gamma Y(2 - Y)$. This one-dimensional wave equation for $m_1'(x, \tau)$ admits free wave solutions

$$m_1'(x, \tau) = \sin x \sin(\omega\tau) \tag{4.7}$$

if and only if the dimensionless wave frequency

$$\omega = \sqrt{1 + \frac{2\Gamma}{3}}; \tag{4.8}$$

i.e. the dimensional sound speed $\tilde{a} = \sqrt{(1 + 2\Gamma/3)\gamma R T_*}$. Thus, the thermal stratification increases the sound speed relative to the unstratified value $a_* = \sqrt{\gamma R T_*}$. Using (4.7), the fluctuating x velocity

$$u_1'(x, Y, \tau) = T_B(Y) \sin x \sin(\omega\tau). \tag{4.9}$$

As anticipated, this velocity component is sheared, exhibiting maximum speeds at the centreline $Y = 1$ where the mean density is least and minimum speeds near the wall $Y = 0$ where the mean density is greatest, owing to the baroclinic production of fluctuating vorticity. Finally, seeking a solution for the fluctuating Y velocity component of the form $V_1'(x, Y, \tau) = F(Y) \cos x \sin(\omega\tau)$ and substituting this ansatz and (4.7) into (4.5) yields an ordinary differential equation for $F(Y)$,

$$\frac{\mathrm{d}F}{\mathrm{d}Y} = -T_B(Y) + \left(1 + \frac{2\Gamma}{3}\right), \tag{4.10}$$

which can be integrated in Y to give

$$V_1'(x, Y, \tau) = \Gamma \left(\frac{2Y}{3} - Y^2 + \frac{Y^3}{3}\right) \cos x \sin(\omega\tau). \tag{4.11}$$

Expression (4.11) confirms that fluctuating wall-normal motions are induced whenever the stratification parameter $\Gamma \neq 0$. Figure 2 shows vector plots of this leading-order acoustic wave velocity field (u_1', V_1') at two instants during a single period that differ in phase by π.

With the leading-order fluctuating velocity components u_1' and V_1' known, the Y-derivative of the RSDs in (4.3) can be readily evaluated, yielding

$$\frac{1}{h^2}\partial_Y^2 \breve{\Omega} = \frac{\Gamma}{2}(Y - 1) \sin(2x). \tag{4.12}$$

From the right-hand side of this equation, we conclude that if $\Gamma = 0$ no streaming at $O(S^{-1})$ is induced. Integrating this equation twice in Y and imposing the stress-free boundary conditions in (2.15) and (2.16) gives an expression for $\breve{\Omega}$, which then can be substituted into (4.4):

$$\partial_Y[T_B(Y)\partial_Y \breve{\Psi}] = -\Gamma h^2 \left(\frac{Y}{6} - \frac{Y^2}{4} + \frac{Y^3}{12}\right) \sin(2x). \tag{4.13}$$

Recalling that the left-hand side of (4.13) is simply $\partial_Y \breve{u}_1 = \partial_Y \bar{u}_1 / Re_s$, it is clear that large-amplitude streaming as measured by $\bar{u}_1 / u_1' = O(Re_s)$ will be realized in the RNW

https://doi.org/10.1017/jfm.2014.61 Published online by Cambridge University Press

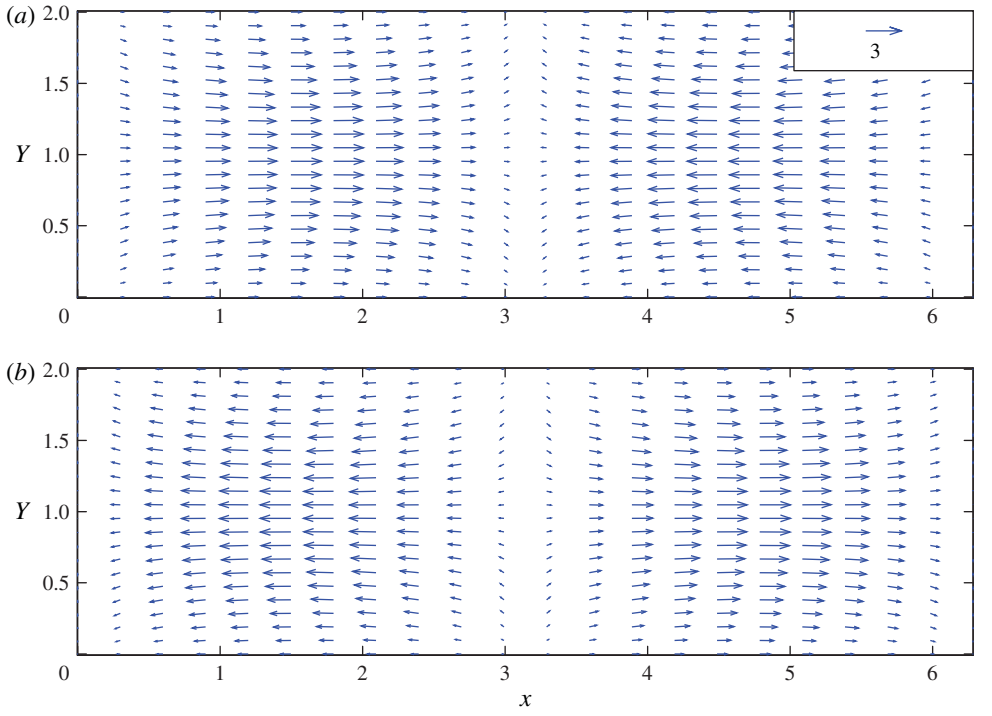


FIGURE 2. (Colour online) Snapshots of the fluctuation velocity field obtained from the small-Pe_s asymptotic theory at two dimensionless times $t = \pi/(2\omega) + n(2\pi/\omega)$ (a) and $t = 3\pi/(2\omega) + n(2\pi/\omega)$ (b), for arbitrary integer n, differing in phase by π. For comparison with the DNS (see figure 5), $\Gamma = 2$ and $h = 1$. The vector fields clearly reveal the presence of a standing *rotational* acoustic wave, as depicted in figure 1.

limit provided $Re_s \gg S^{-1}$, as stipulated (and as is necessary for the validity of the small-(Pe_s, Re_s) theory in its present form).

Although (4.13) is easily integrated once in Y, the x-streaming component $\breve{u}_1$ cannot be completely specified without simultaneously computing the wall-normal streaming speed $\breve{V}_1$ to determine a free x-dependent 'function of integration' $B(x)$. The latter computation involves quadratures of rational functions. Before pursuing this analytical solution, we first demonstrate that $B(x) = B_0 \sin(2x)$, for constant B_0, by formulating a two-point boundary value problem for the mean stream function, which we note can be written as

$$\breve{\Psi}(x, Y) = \phi(Y) \sin(2x) + A(x) \tag{4.14}$$

for some to-be-determined functions $\phi(Y)$ and $A(x)$. Using the relationship between $\breve{V}_1$ and $\breve{\Psi}$ and the no-normal flow boundary and symmetry conditions on $\breve{V}_1$,

$$A(x) = -\phi(0) \sin(2x) = -\phi(1) \sin(2x), \tag{4.15}$$

where an arbitrary constant of integration has been set to zero without loss of generality. Hence,

$$\breve{\Psi}(x, Y) = [\phi(Y) - \phi(0)] \sin(2x) = [\phi(Y) - \phi(1)] \sin(2x) \tag{4.16}$$

https://doi.org/10.1017/jfm.2014.61 Published online by Cambridge University Press

or, upon defining $\Phi(Y) \equiv \phi(Y) - \phi(0) \equiv \phi(Y) - \phi(1)$,

$$\check{\Psi}(x, Y) = \Phi(Y) \sin(2x), \tag{4.17}$$

where crucially $\Phi(0) = \Phi(1) = 0$. Thus,

$$\check{u}_1(x, Y) = T_B(Y) \frac{\mathrm{d}\Phi}{\mathrm{d}Y} \sin(2x). \tag{4.18}$$

Comparing this result with the Y-integral of (4.13) confirms that $B(x) \propto \sin(2x)$, enabling $\check{u}_1$ to be expressed as

$$\check{u}_1(x, Y) = \left\{ -\left(\frac{\Gamma h^2}{12}\right) \left[Y^2 - Y^3 + \frac{Y^4}{4} \right] + B_0 \right\} \sin(2x). \tag{4.19}$$

Substituting (4.17) into (4.13) yields a two-point boundary value problem for $\Phi(Y)$:

$$\frac{\mathrm{d}}{\mathrm{d}Y} \left[T_B(Y) \frac{\mathrm{d}\Phi}{\mathrm{d}Y} \right] = -\Gamma h^2 \left(\frac{Y}{6} - \frac{Y^2}{4} + \frac{Y^3}{12} \right). \tag{4.20}$$

Equation (4.20) can be integrated exactly. Imposition of the homogeneous Dirichlet conditions on $\Phi(Y)$ at $Y = 0, 1$ yields

$$B_0 = \frac{h^2}{48\Gamma} \left(1 - \frac{(1 - 2\Gamma/3)\sqrt{\Gamma(\Gamma+1)}}{\tanh^{-1}\left(\sqrt{\Gamma/(\Gamma+1)}\right)} \right). \tag{4.21}$$

Finally, using (4.17), the mean streaming velocities can be reconstructed:

$$\begin{aligned} \check{u}_1(x, Y) \;=\; & \left\{ \left(\frac{1}{4\Gamma^2}\right) \left(1 - \frac{(1 - 2\Gamma/3)\sqrt{\Gamma(\Gamma+1)}}{\tanh^{-1}\left(\sqrt{\Gamma/(\Gamma+1)}\right)} \right) - \left[Y^2 - Y^3 + \frac{Y^4}{4} \right] \right\} \\ & \times \left(\frac{\Gamma h^2}{12}\right) \sin(2x), \end{aligned} \tag{4.22}$$

$$\check{V}_1(x, Y) \;=\; -\left[1 + \Gamma Y(2 - Y)\right] 2\Phi(Y) \cos(2x), \tag{4.23}$$

where

$$\Phi(Y) = \left(\frac{h^2}{144}\right) \left\{ \frac{(2 - 3/\Gamma) \tanh^{-1}\left[\sqrt{\Gamma/(\Gamma+1)}\,(Y-1)\right]}{\tanh^{-1}\left(\sqrt{\Gamma/(\Gamma+1)}\right)} + 2 - \frac{3}{\Gamma} + \frac{3Y}{\Gamma} - 3Y^2 + Y^3 \right\}. \tag{4.24}$$

Not only does the $O(S^{-1})$ streaming component $\bar{u}_1 = Re_s \check{u}_1$ persist in the RNW limit (again, with $S^{-1} \ll Re_s \ll 1$), but near the (stress-free) walls the streaming is directed *away* from the velocity nodes of the standing acoustic wave, which are located at $x = 0$, π and 2π. Indeed, the near-wall streaming speed

$$\bar{u}_{1w}(x) \sim Re_s \left(\frac{h^2}{48\Gamma}\right) \left[1 - \frac{(1 - 2\Gamma/3)\sqrt{\Gamma(\Gamma+1)}}{\tanh^{-1}\left(\sqrt{\Gamma/(\Gamma+1)}\right)} \right] \sin(2x), \tag{4.25}$$

where the subscript 'w' indicates evaluation at $Y = 0$ or $Y = 2$. Figure 3(*a*) shows the resulting 2D steady streaming flow pattern for $\Gamma = 20$, $Re_s = 0.1$ and $h = 1$. For

https://doi.org/10.1017/jfm.2014.61 Published online by Cambridge University Press

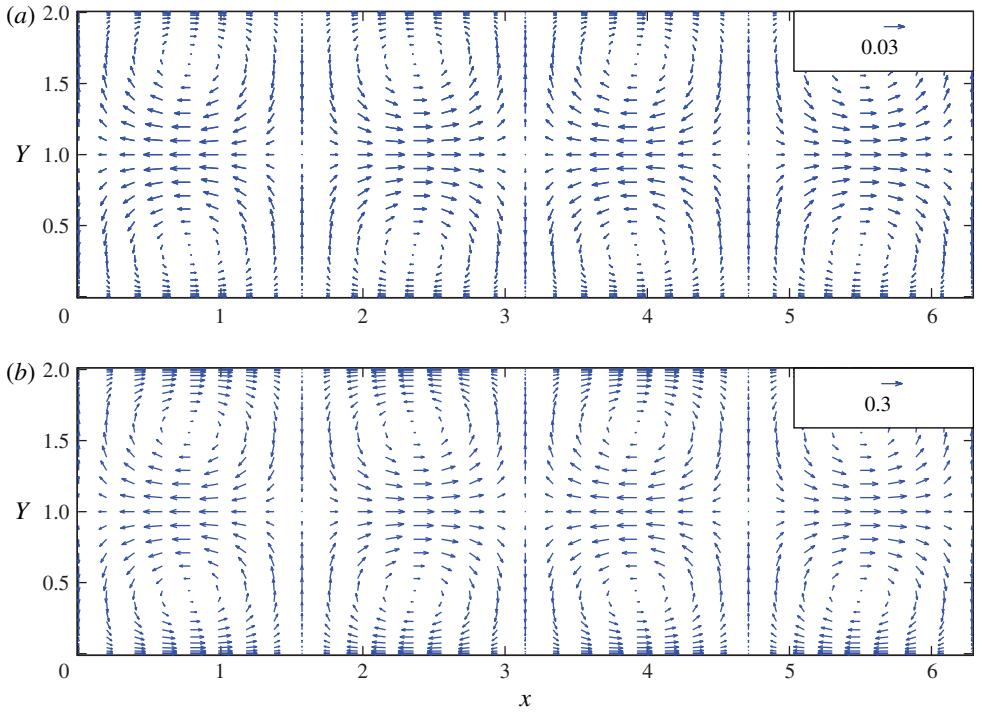


FIGURE 3. (Colour online) Vector plot of theoretically-predicted dimensionless steady-state streaming velocity field $(\bar{u}_1, \bar{V}_1)$ obtained from the analytical formulas (4.22) and (4.23) in the RNW limit of small streaming Reynolds and Péclet numbers, Re_s and Pe_s, recalling $\bar{u}_1 \equiv Re_s \breve{u}_1$ and $\bar{V}_1 \equiv Re_s \breve{V}_1$: (*a*) $\Gamma = 20$, $Re_s = 0.1$ and $h = 1$; (*b*) $\Gamma = 2$, $Re_s = 10\sqrt{7/3}$ and $h = 1$. The parameters for the latter scenario were chosen to match those used in the DNS in § 5, although RNW theory is not expected to be quantitatively reliable in that parameter regime. The streaming flow pattern is broadly similar in both cases. Note in particular that the velocity nodes of the standing acoustic wave are located at $x = 0$, $x = \pi$ and $x = 2\pi$; thus, unlike classical streaming, here the near-wall flow is directed *away* from these velocity nodes.

qualitative comparison with the results of the DNS in § 5, we also show in figure 3(*b*) the streaming flow predicted from (4.22) and (4.23) for $\Gamma = 2$, $Re_s = 10\sqrt{7/3}$ and $h = 1$, although our RNW theory (based on $Re_s \ll 1$) is, of course, not formally valid in this regime.

One virtue of the asymptotic analysis is that various aspects of the streaming physics are made transparent. In particular, the direction of the near-wall streaming flow can be understood. First, note that analytic evaluation of the RSDs in (4.2) shows that the x-divergence is larger in magnitude than the Y-divergence. Focusing on the region $0 \leqslant x \leqslant \pi$ and $0 \leqslant Y \leqslant 1$, the Reynolds stress $-\bar{\rho}_0 \overline{(u_1')^2} \leqslant 0$ is clearly most negative (for given Y) at $x = \pi/2$, since $u_1' \propto \sin x$ and $\bar{\rho}_0$ is x-independent. For $0 < x < \pi/2$ ($\pi/2 < x < \pi$), the x-divergence of this Reynolds stress component is negative (positive); in terms of time-averaged fluxes of fluctuation x-momentum, there is a net outflux of positive fluctuation x-momentum, which is felt by the mean flow as a force acting toward the plane $x = 0$ ($x = \pi$). Since $\bar{\rho}_0 u_1' = m_1'(x, t)$, while $|u_1'(x, Y, t)|$ is maximum (minimum) at the channel centreline (wall) because the

https://doi.org/10.1017/jfm.2014.61 Published online by Cambridge University Press

mean density is minimum (maximum) there (see (4.1)), the magnitude of this effect is greatest near the centreline and least near the wall of the channel. Hence, torques are generated, driving a counterclockwise flow in $0 \leqslant x < \pi/2$ but a clockwise flow in $\pi/2 < x \leqslant \pi$, as evident in figure 3.

We conclude this subsection by observing that although the magnitude of the RNW streaming described here is asymptotically of the same order in *Strouhal number S* as that of the driving acoustic waves, the streaming flow is a factor of Re_s weaker than the fluctuating flow. In the following subsection, we relax this restriction by considering a parameter regime in which the streaming Péclet number remains small, but the streaming Reynolds number is finite.

4.2. *The limit* $S^{-1} \ll Pe_s \ll 1$, $Re_s = O(1)$

We next consider the limit $Pe_s \to 0$ with $Re_s = O(1)$. In this scenario, the streaming Prandtl number is small. Although inappropriate for a pure ideal gas, examination of this limit is instructive for gaining further insight into the streaming behaviour admitted by our mathematical model, and mixtures of noble gases with moderately small Prandtl numbers (e.g. $\approx$0.17) are, in fact, realizable (Bajaj, Ahlers & Pesch 2002; Tijani, Zeegers & de Waele 2002).

Since $Pe_s \ll 1$, steady solutions with $\bar{\Theta}_0 = 0$ can again be sought, in which case the fluctuations again decouple from the mean flow. Thus, the leading-order (in S) fluctuating velocity components are still given by (4.9) and (4.11), enabling the Reynolds stress forcing to be evaluated analytically. Relative to the RNW limit just considered, the only change in the equations governing the mean dynamics is that mean (nonlinear) inertia terms must be retained in (4.2) and therefore in (4.3). The resulting system in steady-state, stream-function/vorticity form is

$$\begin{aligned}\partial_Y\bar{\Psi}\,\partial_x\bar{\Omega} - \partial_x\bar{\Psi}\,\partial_Y\bar{\Omega} &= \partial_Y[\partial_x(\bar{\rho}_0\overline{u_1'^2}) + \partial_Y(\bar{\rho}_0\overline{V_1'u_1'})] \\ &\quad + \left(\frac{1}{2\bar{\rho}_0^2}\right)\partial_Y\bar{\rho}_0\,\partial_x[(\partial_Y\bar{\Psi})^2] + \frac{1}{Re_s h^2}\partial_Y^2\bar{\Omega} \\ &= \frac{\Gamma}{2}(1-Y)\sin 2x + \left(\frac{1}{2\bar{\rho}_0^2}\right)\partial_Y\bar{\rho}_0\,\partial_x[(\partial_Y\bar{\Psi})^2] \\ &\quad + \frac{1}{Re_s h^2}\partial_Y^2\bar{\Omega}, \qquad (4.26)\end{aligned}$$

$$\partial_Y\left(\frac{1}{\bar{\rho}_0}\partial_Y\bar{\Psi}\right) = -\bar{\Omega}, \qquad (4.27)$$

where $\bar{\Omega} \equiv -\partial_Y\bar{u}_1$, $\bar{\rho}_0\bar{u}_1 \equiv \partial_Y\bar{\Psi}$ and $\bar{\rho}_0\bar{V}_1 \equiv -\partial_x\bar{\Psi}$.

For arbitrary Re_s, the system (4.26)–(4.27) must be solved numerically. The results of one such computation, performed by marching a Fourier–Chebyshev pseudospectral code with semi-implicit time-stepping to steady state, are depicted in figure 4, which shows a plot of the resulting 2D steady streaming flow. For this representative case, for which the parameters (apart from Pe_s) were again chosen to match those used in the DNS, i.e. $\Gamma = 2$, $Re_s = 10\sqrt{7/3}$ and $h = 1$, we find that $\bar{u}_{1\max}/u'_{1\max} \simeq 0.3/3 = 0.1$. Moreover, the near-wall streaming flow is again seen to be directed away from the velocity nodes of the standing acoustic wave at $x = 0$, π and 2π.

Collectively, these results confirm that the hypothesized mechanism for large-amplitude acoustic streaming proposed here can, in fact, enable conditions (*b*), (*d*)

https://doi.org/10.1017/jfm.2014.61 Published online by Cambridge University Press

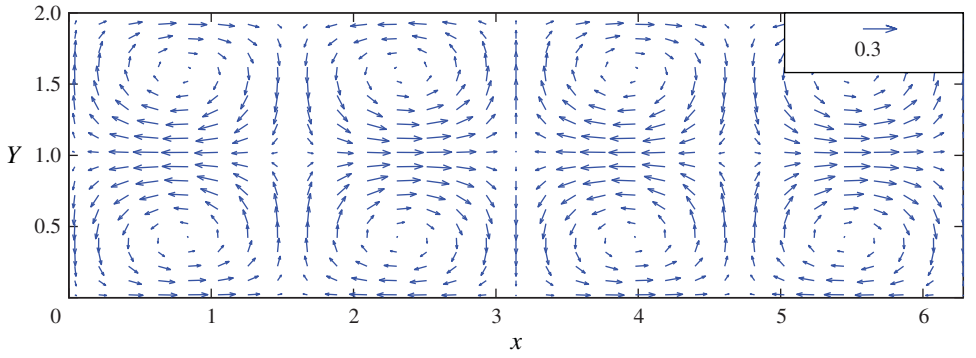


FIGURE 4. (Colour online) Vector plot of dimensionless steady-state streaming velocity field $(\bar{u}_1,\ \bar{V}_1)$ obtained by numerically solving (4.26)–(4.27) for $\Gamma = 2$, $Re_s = 10\sqrt{7/3}$ and $h = 1$. The velocity nodes of the standing acoustic wave are located at $x = 0$, $x = \pi$ and $x = 2\pi$. Unlike classical streaming, the near-wall flow is directed *away* from these velocity nodes. For reference, the maximum (dimensionless) fluctuation velocity $u'_{1\max}$ is 3 and occurs along the channel centreline.

and (*e*) enumerated in § 1 to be relaxed, as is evidently necessary to explain streaming in HID lamps and as may be important in other thermo-acoustic systems.

5. DNS

To corroborate our streaming theory, we performed DNS of the dimensionless system (2.9)–(2.13) but with the dimensional wall-parallel *and* wall-normal coordinates and velocity components ($\tilde{x}$, $\tilde{y}$ and $\tilde{u}$, $\tilde{v}$) and pressure perturbation $\tilde{\pi}$ scaled using the dimensional wavenumber k_* and particle speed U_* of the acoustic waves (yielding dimensionless variables x, y and $\hat{u} \equiv Su \sim u_1$, $\hat{v} \equiv Sv \equiv \delta SV \sim \delta V_1$) and pressure scale $\rho_* a_* U_*$ (yielding dimensionless pressure perturbation $\hat{\pi} \equiv S\pi/\gamma \sim \pi_1/\gamma$), respectively. The equations were solved using OpenFOAM (Open Source Field Operation and Manipulation) software, which comprises various numerical libraries and ready-to-use subroutines (OpenFOAM 2009) and which has been used effectively in a diverse array of challenging applications (e.g. Malecha *et al.* 2011). For the present application, a finite-volume discretization was employed in conjunction with the PISO (Pressure Implicit with Splitting of Operators) algorithm for compressible flows (Issa, Gosman & Watkins 1986; Ferziger & Peric 1999). Like the widely-used SIMPLE (Semi-Implicit Method for Pressure Linked Equations) algorithm, PISO schemes belong to the family of pressure correction methods. However, the PISO method requires less computational effort, as conservation of mass is satisfied within predictor–corrector steps, thereby obviating the need for iteration.

The computational domain, $0 \leqslant x \leqslant 2\pi$ and $0 \leqslant y \leqslant \delta$, represented one-half of the channel. Periodicity boundary conditions were enforced at $x = 0,\ 2\pi$, while $\partial_y \hat{u} = \hat{v} = \partial_y \hat{\pi} = \partial_y \Theta = 0$ along the lower wall $y = 0$ and channel centreline $y = \delta$. The flow was initialized by prescribing the following conditions on the *total* (i.e. mean plus fluctuation) fields at an arbitrary initial time $t_0 = \pi/(2\omega)$ (where $\omega = \sqrt{1 + 2\Gamma/3}$):

$$\hat{u}(x, y, t_0) = T_b(y) \sin x; \quad \hat{v}(x, y, t_0) = \delta f(y) \cos(x); \quad \hat{\pi}(x, y, t_0) = \Theta(x, y, t_0) = 0, \tag{5.1}$$

where $T_b(y) = T_B(Y)$ and $f(y) = F(Y)$. For the DNS discussed below, $\Gamma = 2$, $Re_s = 10\sqrt{1 + 2\Gamma/3} = 10\sqrt{7/3}$ (recall that $Re = SRe_s$, however), $\gamma = 3/2$, and

https://doi.org/10.1017/jfm.2014.61 Published online by Cambridge University Press

$h = 1$. Motivated in part by the use of noble gas mixtures in HID lamps and in part by the analysis performed in § 4, we set the Prandtl number to 0.1, implying $Pe_s = \sqrt{1 + 2\Gamma/3} = \sqrt{7/3}$ (i.e. $Pe_s = Re_s/10$ and $Pe = Re/10$). All fields are plotted in the rescaled (x, Y) domain to facilitate comparisons with the theoretical results of the previous section.

To investigate the dependence of the induced streaming flows on the Strouhal number, simulations were performed for $S = 250/\omega$, $500/\omega$, $1000/\omega$ and $2000/\omega$, and the resulting flows were diagnosed at dimensionless times in the neighbourhood of $t \simeq S$ and $t \simeq 2S$. Decomposition of the total flow into mean (streaming) and fluctuating (wave) parts was accomplished by time-averaging the x- and y-velocity components within a $\Delta t = 10\pi/\omega$ time window approximately centred on $t_a + \Delta t/2 \simeq S$ or $t_a + \Delta t/2 \simeq 2S$. (Hence, for $S = 1000/\omega$ and $t_a \simeq S - \Delta t/2$, for example, the time-averaging period was chosen to be $975.46 \leqslant \omega t \leqslant 975.46 + 10\pi$.) Thus, for the DNS, we define

$$\bar{u}(x, y; t_a, \Delta t) \equiv \frac{1}{\Delta t} \int_{t=t_a}^{t=t_a+\Delta t} \hat{u}(x, y, t)\, \mathrm{d}t \tag{5.2}$$

and similarly for $\bar{v}$. The fluctuating velocity components are then defined as $u' \equiv \hat{u} - \bar{u}$ and $v' \equiv \hat{v} - \bar{v}$. Figure 5 shows the fluctuating velocity field computed in this way at two instants ($\omega t \simeq 1001.66$ and $\omega t \simeq 1004.86$) for $S = 1000/\omega$. As expected, these snapshots reveal a standing acoustic wave pattern with a phase difference approximately equal to π. Moreover, the x-directed velocity is sheared in the y direction, confirming the presence of strong fluctuating vorticity within the interior of the domain. This vorticity is generated by fluctuating baroclinic torques that are associated with the roughly orthogonal mean isopycnals and fluctuating isobars, as depicted in figure 1.

The corresponding mean flow, plotted in figure 6, clearly exhibits the same spatial pattern and approximately the same magnitude as that predicted by the asymptotic analysis and shown in figures 3(*b*) and 4. In particular, the near-wall streaming is directed away from the acoustic-wave velocity nodes located at $x = 0$, $x = \pi$ and $x = 2\pi$ (cf. figure 5). In figure 7, the theoretically predicted and numerically simulated streaming speeds along the channel centreline ($Y = 1$) are compared directly. Although the mean flow extracted from the DNS is roughly 15 % weaker than the theoretical prediction, the streaming magnitudes are comparable, providing strong confirmation of the theory. The modest quantitative differences may be attributed to several factors: (i) the acoustic waves are weakly damped in the DNS but not in the (leading-order) theory; (ii) the mean flows extracted from the DNS depend weakly on the averaging period Δt and averaging time t_a; and (iii) fully two-way coupling between the waves and induced mean flows is likely occurring in the DNS, since $Pe_s = O(1)$, but is not treated in the theory.

Given these factors, the crucial quantitative test of the theory is not so much the numerical magnitude of the simulated mean flow but, rather, the dependence, or not, of the ratio of the typical mean to fluctuation flow speed on the Strouhal number S. A cornerstone of the theory is that this ratio is asymptotically $O(1)$, that is, S-independent, for large-amplitude streaming.

We proceed by using spatial averaging to define a representative scalar streaming speed $\bar{u}_m$:

$$\bar{u}_m \equiv \frac{1}{2\pi\delta} \int_0^{\delta} \int_0^{2\pi} \sqrt{\bar{u}^2 + \bar{v}^2}\, \mathrm{d}x\, \mathrm{d}y \sim \frac{1}{2\pi\delta} \int_0^{\delta} \int_0^{2\pi} |\bar{u}|\, \mathrm{d}x\, \mathrm{d}y, \tag{5.3}$$

https://doi.org/10.1017/jfm.2014.61 Published online by Cambridge University Press

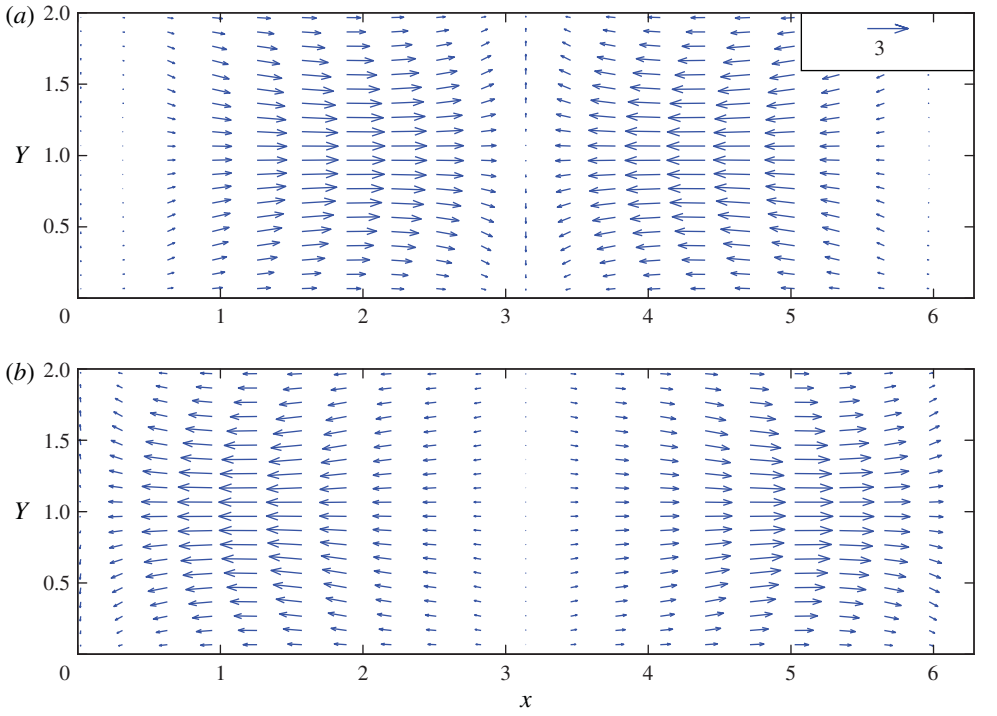


FIGURE 5. (Colour online) Snapshots of the fluctuation velocity field obtained from the DNS at dimensionless times $\omega t \simeq 1001.66$ (upper) and $\omega t \simeq 1004.86$ (lower) for $S = 1000/\omega$, $\Gamma = 2$, $\gamma = 3/2$, $h = 1$, $\delta = 1/\sqrt{S}$ and $Re_s = 10Pe_s = 10\sqrt{7/3}$. The vector fields clearly reveal the presence of a standing *rotational* acoustic wave, as depicted in figure 1. These results may be compared directly with the theoretically predicted fluctuation velocity field shown in figure 2.

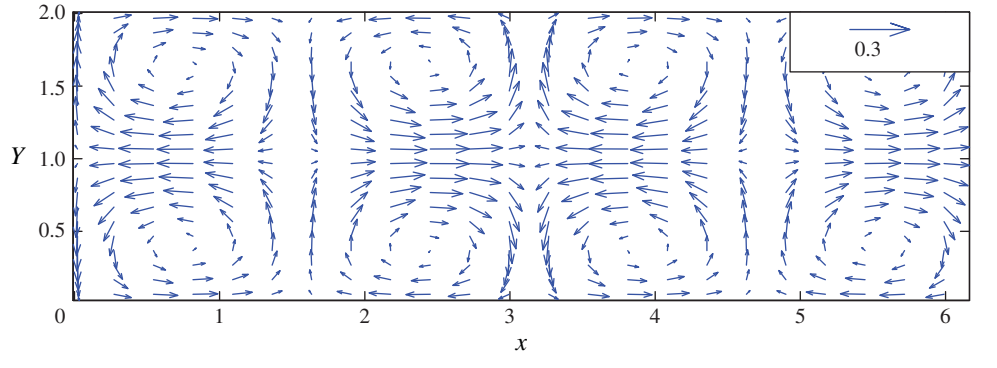


FIGURE 6. (Colour online) Streaming velocity field $(\bar{u}, \bar{V})$ obtained from the DNS for $S = 1000/\omega$, $\Gamma = 2$, $\gamma = 3/2$, $h = 1$, $\delta = 1/\sqrt{S}$ and $Re_s = 10Pe_s = 10\sqrt{7/3}$ and time-averaging period $975.46 \leqslant \omega t \leqslant 975.46 + 10\pi$ (cf. the corresponding theoretical prediction shown in figures 3(*b*) and 4).

since $\bar{v} = O(\delta)$. A typical fluctuation speed u'_m during the time-averaging period was computed in two steps. First, a phase (or ensemble) average of the *total* velocity

https://doi.org/10.1017/jfm.2014.61 Published online by Cambridge University Press

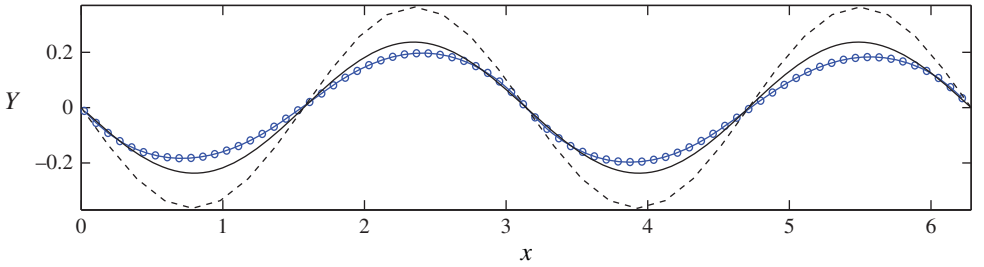


FIGURE 7. (Colour online) Comparison of streaming velocity $\bar{u}_1(x, Y = 1)$ predicted by the asymptotic theory (solid curve, extracted from figure 4, and dashed curve, extracted from figure 3(*b*)) with the corresponding mean flow profile $\bar{u}(x, Y = 1)$ extracted from the DNS (and denoted with circles) for $S = 1000/\omega$, $\Gamma = 2$, $\gamma = 3/2$, $h = 1$, $\delta = 1/\sqrt{S}$ and $Re_s = 10Pe_s = 10\sqrt{7/3}$ and averaging time $975.46 \leqslant \omega t \leqslant 975.46 + 10\pi$.

ωS	250	500	1000	2000
ωt	250	500	1000	2000
$\bar{u}_m$	0.055	0.067	0.07	0.065
u_m	1.137	1.216	1.332	1.410
u'_m	1.082	1.149	1.262	1.344
$\bar{u}_m/u'_m$	0.051	0.058	0.056	0.049

TABLE 3. Ratio of typical mean to fluctuation speed in DNS for $t \simeq S$.

ωS	250	500	1000	2000
ωt	500	1000	2000	4000
$\bar{u}_m$	0.049	0.072	0.86	0.090
u_m	1.09	1.33	1.361	1.556
u'_m	1.041	1.258	1.275	1.466
$\bar{u}_m/u'_m$	0.047	0.057	0.067	0.061

TABLE 4. Ratio of typical mean to fluctuation speed in DNS for $t \simeq 2S$.

field was performed by summing the 10 velocity fields exhibiting maximum flow speeds (with one peak observed roughly every $4/\omega$ time units during the $\Delta t = 10\pi/\omega$ window) and dividing by 10. Next, a scalar metric u_m of the total velocity was obtained via spatial averaging, in precise analogy with (5.3). The representative scalar *fluctuation* speed was then defined to be $u'_m \equiv u_m - \bar{u}_m$. The results of this data analysis are summarized in tables 3 and 4. Crucially, in each case, the ratio $\bar{u}_m/u'_m$ maintains an approximate value of 0.05 over almost an order of magnitude variation in S, in accord with the theoretical prediction. By contrast, were classical Rayleigh streaming responsible for the mean flows computed in the DNS, the corresponding ratio would exhibit an almost 10-fold decrease as S was increased from $250/\omega$ to $2000/\omega$.

6. Discussion

Motivated by acoustic streaming in HID lamps, we have performed an asymptotic analysis and DNS of an idealized flow comprising standing acoustic waves in a

https://doi.org/10.1017/jfm.2014.61 Published online by Cambridge University Press

density-stratified gas in a channel. The analysis is made tractable not only by making high-frequency and long-wavelength approximations but also by decoupling the leading-order acoustic wave dynamics from the induced streaming flow. This latter simplification is effected by considering the limit of small streaming Péclet number, which enables the mean temperature distribution in the channel to maintain a prescribed functional form (parabolic in the cross-channel coordinate and streamwise-independent) and strictly steady streaming solutions to be found.

With these simplifications, we demonstrate the occurrence of acoustic streaming flows that differ fundamentally from those predicted by classical analyses. Specifically, strong acoustic streaming can be generated by fluctuating baroclinic torques acting in the interior of the flow domain. Owing to the baroclinic generation mechanism, the amplitude of the streaming flow is controlled by the relative magnitudes of the normalized background density gradient Γ and streaming Reynolds number Re_s. For $\Gamma = O(1)$ and $Re_s \geqslant O(1)$, streaming speeds comparable to acoustic-wave induced velocity fluctuations are attained, *independently* of the Strouhal number S. Our theoretical predictions are corroborated by DNS, which, for the given parameter values $\Gamma = 2$, $\gamma = 3/2$, $h = 1$ and $Re_s = 10Pe_s = 10\sqrt{7/3}$, show that wall-parallel streaming speeds reach approximately 5 % of the characteristic fluctuation speed, again independently of S. In the case of HID streaming, for which $S \approx 10^3$ and fluctuation speeds reach 3 m s^{-1}, the dimensional magnitude of the observed mean flows ($\simeq$30 cm s^{-1}) is consistent with the theoretically predicted and numerically simulated streaming speeds identified here ($\simeq$20 cm s^{-1}). By contrast, classical Rayleigh streaming flows would only reach 0.3 cm s^{-1}, orders of magnitude too small to explain the observed behaviour in HID lamps (Dreeben & Chini 2011).

Our analysis also substantiates the assertion made in Dreeben & Chini (2011) that baroclinically driven acoustic streaming dominates any boundary-layer induced streaming in the neighbourhood of a no-slip boundary. At the edge of the boundary layer, the latter is directed *toward* the velocity nodes (e.g. toward $x = 0$), in contrast with observations and experiments of HID streaming and with the streaming flows analysed in this paper.

As discussed in § 1, Riley (2001) enumerates three distinct physical scenarios that can lead to steady streaming. Of these, two need *not* involve the action of viscosity, flows with fluctuating non-conservative body forces (e.g. g-jitter-induced buoyancy fluctuations) and oscillatory flows with free surfaces, but only the former can give rise to *strong* streaming (Riley & Trinh 2001). Our analysis clearly identifies sufficient, although perhaps not necessary, conditions for strong *acoustic* streaming even in the absence of non-conservative body forces: (i) the baroclinic generation of $O(1)$ fluctuating interior vorticity in response to a given boundary-parallel fluctuating pressure gradient, owing to wall-normal time-mean density variations; and (ii) a suitable geometric (or other) constraint that forces the time-mean pressure distribution to be independent of the wall-normal coordinate.

In summary, we have identified a scientifically and technologically important class of large-amplitude baroclinically-driven acoustic streaming flows. Future work will focus on incorporating (mean and fluctuating) buoyancy effects into the analysis, which could yield an additional mechanism for streaming in HID lamps. More significantly, the fully coupled wave/mean-flow interaction problem, in which the mean density gradient is modified by the streaming flow, will be properly treated. Analysis of the resulting multiple time-scale system may provide guidelines for the design of new control algorithms for stabilizing the arc regions in HID lamps, with important ramifications for energy efficiency.

https://doi.org/10.1017/jfm.2014.61 Published online by Cambridge University Press

Acknowledgements

The authors would like to express their gratitude to the referees for their constructive comments and suggestions. GPC would also like to acknowledge support from the annual Woods Hole summer program in Geophysical Fluid Dynamics, where much of the analysis was completed.

REFERENCES

ABDULLE, A. & E, W. 2003 Finite-difference heterogeneous multi-scale method for homogenization problems. *J. Comput. Phys.* **191** (1), 18–39.

AMIN, N. 1988 The effect of g-jitter on heat transfer. *Proc. R. Soc. Lond.* A **419**, 151–172.

BAJAJ, K., AHLERS, G. & PESCH, W. 2002 Rayleigh–Bénard convection with rotation at small Prandtl numbers. *Phys. Rev.* E **65**, 056309: 1–13.

BATCHELOR, G. K. 1973 *An Introduction to Fluid Dynamics*. 1st edn. Cambridge University Press, Cambridge.

CHUNG, S. K. & TRINH, E. H. 1998 Containerless protein crystal growth in rotating levitated drops. *J. Cryst. Growth* **194**, 384–397.

DAVIDSON, B. J. 1973 Heat transfer from a vibrating cylinder. *Intl J. Heat Mass Transfer* **76**, 1703–1727.

DREEBEN, T. D. 2008 Modelling of fluid-mechanical arc instability in pure-mercury HID lamps. *J. Phys.* D **41**, 144023.

DREEBEN, T. D. & CHINI, G. P. 2011 Two-dimensional streaming flows in high-intensity discharge lamps. *Phys. Fluids* **23**, 056101.

FERZIGER, J. H. & PERIC, M. 1999 *Computational Methods for Fluid Dynamics*. Springer.

GAVER, D. P. & GROTBERG, J. B. 1986 An experimental investigation of oscillating flow in a tapered channel. *J. Fluid Mech.* **172**, 47–61.

GOPINATH, A. & MILLS, A. F. 1993 Convective heat transfer from a sphere due to acoustic streaming. *ASME J. Heat Transfer* **115**, 332–341.

GROTBERG, J. B. 1984 Volume-cycled oscillatory flow in a tapered channel. *J. Fluid Mech.* **141**, 249–264.

ISSA, R. I., GOSMAN, A. D. & WATKINS, A. P. 1986 The computation of compressible and incompressible recirculating flows by a non-iterative implicit scheme. *J. Comput. Phys.* **62** (1), 66–82.

LIGHTHILL, M. J. 1978 Acoustic streaming. *J. Sound Vib.* **61**, 391–418.

LIGHTHILL, M. J. 1991 Biomechanics of hearing sensitivity. *ASME J. Vib. Acoust.* **113**, 1–13.

LIGHTHILL, M. J. 1992 Acoustic streaming in the ear itself. *J. Fluid Mech.* **239**, 551–606.

MALECHA, Z., CHINI, G. P. & JULIEN, K. 2013 A multiscale algorithm for simulating spatially-extended Langmuir circulation dynamics. *J. Comput. Phys.* in press, http://dx.doi.org/10.1016/j.jcp.2013.07.003.

MALECHA, Z., MIROSLAW, L., TOMCZAK, T., KOZA, Z., MATYKA, M., TARNAWSKI, W. & SZCZERBA, D. 2011 GPU-based simulation of 3D blood flow in abdominal aorta using OpenFOAM. *Arch. Mech.* **63** (2), 137–161.

MEI, C. C. 1985 Resonant reflection of surface water waves by periodic sandbars. *J. Fluid Mech.* **152**, 315–335.

MERKIN, J. H. 1967 Oscillatory free convection from an infinite horizontal cylinder. *J. Fluid Mech.* **30**, 561–575.

NYBORG, W. L. 1953 Acoustic streaming due to attenuated plane waves. *J. Acoust. Soc. Am.* **25**, 68–75.

OpenFOAM 2009 The Open Source CFD Toolbox User Guide. Free Software Foundation.

PIERCY, J. E. & LAMB, J. 1954 Acoustic streaming in liquids. *Proc. R. Soc. Lond.* A **226**, 43–50.

RAYLEIGH, 1883 On the circulation of air observed in Kundt's tubes and some allied acoustical problems. *Trans. R. Soc.* **75**, 1–21.

RILEY, N. 2001 Steady streaming. *Annu. Rev. Fluid Mech.* **33**, 43–65.

https://doi.org/10.1017/jfm.2014.61 Published online by Cambridge University Press

RILEY, N. & TRINH, E. H. 2001 Steady streaming in oscillatory inviscid flow. *Phys. Fluids* **13**, 1956–1960.

STOCKWALD, A., KAESTLE, H. & WEISS, H. 2008 Significant efficacy enhancement of low wattage metal halide HID lamp systems by acoustically induced convection configuration. *IEEE 35th International Conference on Plasma Science, 2008 (ICOPS 2008), Karlsruhe, Germany*. IEEE Press.

TIJANI, M. E. H., ZEEGERS, J. C. H. & DE WAELE, A. T. A. M. 2002 Prandtl number and thermoacoustic refrigerators. *J. Acoust. Soc. Am.* **112**, 134–143.

WESTERVELT, P. J. 1953 The theory of steady rotational flow generated by a sound field. *J. Acoust. Soc. Am.* **25**, 60–67.

WITTING, H. L. 1978 Acoustic resonances in cylindrical high-pressure arc discharges. *J. Appl. Phys.* **49**, 2680–2683.

WYBROW, M. F. & RILEY, N. 1996 Oscillatory flow over a cylinder resting on a plane boundary. *Eur. J. Appl. Maths* **7**, 545–558.

https://doi.org/10.1017/jfm.2014.61 Published online by Cambridge University Press